The Occurrence of Particle Size Distribution Bimodality in Midlatitude Cirrus as Inferred from Ground-Based Remote Sensing Data

YANG ZHAO

Department of Electrical Engineering, University of Utah, Salt Lake City, Utah

GERALD G. MACE

Department of Atmospheric Sciences, University of Utah, Salt Lake City, Utah

JENNIFER M. COMSTOCK

Pacific Northwest National Laboratory, Richland, Washington

(Manuscript received 16 October 2009, in final form 1 October 2010)

ABSTRACT

Data collected in midlatitude cirrus clouds by instruments on jet aircraft typically show particle size distributions that have distinct distribution modes in both the 10–30-μm maximum dimension (D) size range and the 200–300-μm D size range or larger. A literal interpretation of the small D mode in these datasets suggests that total concentrations N_t in midlatitude cirrus are, on average, well in excess of 1 cm^{-3} whereas more conventional analyses of in situ data and cloud process model results suggest N_t values a factor of 10 less. Given this wide discrepancy, questions have been raised regarding the influence of data artifacts caused by the shattering of large crystals on aircraft and probe surfaces. This inconsistency and the general nature of the cirrus particle size distribution are examined using a ground-based remote sensing dataset. An algorithm using millimeter-wavelength radar Doppler moments and Raman lidar-derived extinction is developed to retrieve a bimodal particle size distribution and its uncertainty. This algorithm is applied to case studies as well as to 313 h of cirrus measurements collected at the Atmospheric Radiation Measurement site near Lamont, Oklahoma, in 2000. It is shown that particle size distributions in cirrus can often be described as bimodal, and that this bimodality is a function of temperature and location within cirrus layers. However, the existence of $N_t > 1$ cm^{-3} in cirrus is rare (<1% of the time) and the N_t implied by the remote sensing data tends to be on the order of 100 cm^{-3}.

1. Introduction

Cirrus clouds play an important role in regulating the earth's energy budget through their interactions with solar and terrestrial radiation. Because cirrus cover large areas of the tropics (Mace et al. 2009) and they absorb upwelling thermal radiation, they can significantly influence the thermal structure of the atmosphere. To better understand the feedbacks of cirrus on the climate system, it is necessary to understand the processes that control the evolution of the macrophysical and microphysical cloud properties. This chain of understanding must be based on a foundation of reliable measurements of cirrus particle size distributions (PSDs) and the bulk properties of the PSD such as condensed water content (IWC), extinction, mean particle size, and total particle concentration N_t.

Because the bulk characteristics of cirrus are derived from PSDs that in turn depend on a coupling between the dynamics and thermodynamics with microphysical processes, a great deal of theoretical and observational work has been devoted to defining the characteristic cirrus bulk properties in terms of their microphysics. It has been recognized for some time that bimodality is often a defining feature of cirrus PSDs where a small particle mode often exists in the sub-100-μm size range and a larger particle mode exists at sizes in excess of several hundred microns (e.g., Varley 1978). Platt (1997) found it necessary to assume bimodality in the cirrus PSDs to parameterize the visible extinction in terms of the IWC. Mitchell et al. (1996) provided an early theoretical treatment of this topic finding that aggregation processes and

Corresponding author address: Gerald G. Mace, Department of Atmospheric Sciences, University of Utah, 135 S 1460 E, Rm 819, Salt Lake City, UT 84112.
E-mail: jay.mace@utah.edu

DOI: 10.1175/2010JAS3354.1

depositional growth due to enhanced ventilation were important for describing the evolution of bimodal cirrus PSDs. More recent work by Khvorostyanov and Curry (2008a,b), who build on prior work by Khvorostyanov and Sassen (1998a,b), provides firm theoretical underpinning for the occurrence of bimodal size distributions. They show that bimodality evolves naturally within ice clouds due to normal condensational growth and sedimentation even in regions where relative humidities are subsaturated with respect to ice.

Observational evidence for bimodality in cirrus PSDs derived from analysis of Optical Array Probes (OAPs) such as the Particle Measurement Systems (PMS) Forward Scattering Spectrometer Probe (FSSP) that could count particles smaller than 100 μm suggested that interpretation of earlier in situ measurements that did not consider sub-100-μm particles significantly undercounted N_t (e.g., Arnott et al. 1994). This thinking was supported by data collected over diverse geographical regions in cirrus by Gayet et al. (2002), who reported that N_t values in excess of 5 cm^{-3} are common in midlatitude cirrus. Lawson et al. (2006) supported this finding. Based on observational evidence, Ivanova et al. (2001) developed a parameterization for general circulation models that represented the bimodality suggested by the FSSP. Recently, Mitchell et al. (2008) examined the radiative impact that significantly bimodal PSDs would have within the climate system by implementing two versions of the Ivanova et al. (2001) parameterization in version 3 of the Community Atmosphere Model (CAM3). They found by analyzing 1-yr integrations of the model using observed sea surface temperatures that the vertically integrated global ice mass or ice water paths (IWP)] and the global cirrus cloud fraction increased by 12% and 5.5% with locally much larger increases in the tropics where the shortwave and longwave cloud radiative forcing increased by more than 50%. These changes resulted from the increased longevity of cirrus when more of the condensed mass is assumed to exist in the small PSD mode, significantly decreasing the sedimentation rates and effectively increasing cloud lifetimes.

Other observational studies cast doubt on the prevalence and implied radiative importance of small ice crystals. Heymsfield and McFarquhar (1996) found that the highly reflective nature of tropical cirrus was not due to small ice crystals, as implied in the Ivanova et al. parameterization. More recent studies suggested that in situ measurements from the FSSP or the Cloud Aerosol and Precipitation Spectrometer (CAPS) may be contaminated by ice crystal shattering on probe inlets. Field et al. (2003) showed that the ice particle interarrival times measured by a fast FSSP can be characterized by a Markov chain model with two independent Poisson processes, and that the debris from ice crystal shattering and the unaffected particles may be the sources for these two different Poisson processes. Korolev and Isaac (2005) demonstrate two possible physical mechanisms for the ice crystal shattering: mechanical impact with the probe arms and interaction with the aerodynamic field around the probe housing. Heymsfield (2007) further investigated the shattering effects on measurements from the Cloud and Aerosol Spectrometer (CAS) and the Cloud Integrating Nephelometer (CIN) as well as the FSSP and suggested that the contribution from shattered artifacts on FSSP and CIN measurements is significant for optical extinction measurements. Using in situ measurements from the Tropical Warm Pool International Cloud Experiment (TWP-ICE), McFarquhar et al. (2007) showed that the number concentrations of particles between 3 and 50 μm measured by the CAS with an inlet are nearly a factor of 100 larger than those from the Cloud Droplet Probe (CDP), which does not have an inlet and thus has no effect from the inlet shattering. Jensen et al. (2009) used advanced OAP probes such as the Two-Dimensional Stereo Probe (2DS; Lawson et al. 2006) that could discriminate shattering events from natural particles using particle interarrival times. They report that enhancements to N_t could be as great as a factor of 10 under conditions where large particles were present. Finally, Mitchell et al. (2010) analyzed satellite data using the difference in 11- and 12-μm emissivity to retrieve concentrations of small particles. They conclude that the ubiquitous occurrence of high concentrations of small ice crystals reported by aircraft instruments appears to be erroneous but that occasional bimodality of cirrus PSDs does occur.

This discussion motivates the two related issues that we would like to address with this study. While there is sound theoretical evidence for the occurrence of bimodal PSDs in cirrus, there has been an ongoing disagreement in the cirrus research community regarding the contribution of the small particle mode to cirrus bulk properties with that argument being derived principally from data collected in situ. Following Mitchell et al. (2010) we examine remote sensing data to shed light on this issue except that we use a ground-based dataset consisting of extinction derived from Raman lidar combined with coincident Doppler velocity and radar reflectivity measured by Ka-band Doppler radar. We assume, as did Ivanova et al. (2001) and others, that cirrus particle size distributions can be described by two independent modified gamma functions that describe a small particle mode and a larger particle mode. We make no a priori assumption regarding the concentrations of small particles but we contend that if their ubiquity is indeed true, then remote sensing data must be consistent with that ubiquity. In any case, a proper analysis of the data should shed light on the frequency and significance of bimodality in these clouds.

2. Algorithm development

There have been several lidar–radar cirrus cloud property retrieval algorithms presented in the literature (Okamoto et al. 2003; Wang and Sassen 2002; Stephens et al. 2002); however, Donovan (2003) is the only one to have assumed a bimodal PSD in a lidar–radar retrieval algorithm where he examined effective particle size. We allow for the possibility that the PSD of a cirrus volume could have distinct populations of small and large particles (i.e., bimodality) where those populations may be entirely unrelated to one another. The bimodal size distribution assumption has been used in previous applications such as in cirrus cloud models (Mitchell 1996) and also in the parameterization of visible extinction for ice clouds (Platt 1997). In the algorithm developed here, two modified gamma functions are used to approximate small and large particle modes:

$$N(D) = N_l(D) + N_s(D) = \sum_{x=l,s} A_x \left(\frac{D}{D_{g,x}}\right)^{\alpha_x} \exp\left(\frac{D - D_{g,x}}{D_{g,x}}\right), \quad (1)$$

where subscript x stands for the large particle mode l and the small particle mode s, D is the particle maximum dimension, $D_{g,x}$ is the distribution parameter that controls the slope of the distribution, A_x is the number of particles per unit volume per unit length at the size $D_{g,x}$, and α_x is the parameter that controls the breadth of the distribution.

The algorithm is formulated in terms of the liquid water equivalent radar reflectivity factor Z_e, the Doppler velocity V_d observed at a wavelength that is large with respect to D, and the optical extinction β_{ext} derived at a wavelength that is small with respect to D. Here Z_e provides information that is strongly weighted to the largest particles in $N(D)$; when a prominent large particle mode is present, it can be nearly entirely determined by it. The β_{ext} is determined by the second moment of $N(D)$ and, when a prominent small mode is present, this quantity can be nearly entirely described by the small-mode PSD. Because the particle terminal velocity depends on the ratio of the mass to cross-sectional area (Heymsfield 1972; Mitchell 1996), V_d provides something of a link between the extinction and the mass of the PSD.

a. Forward model equations

Here Z_e can be expressed as

$$Z_e = \int a_z N(D) D^{b_z+6}\, dD, \quad (2)$$

where a_z and b_z are power-law parameters fit to the radar backscattering cross section from ice crystals. Following Deng and Mace (2006; hereafter DM06), the power-law parameters a_z and b_z can be expressed in terms of the coefficient a_m and b_m in a mass–dimensional power-law relationship $m = a_m D^{b_m}$ as

$$a_z = \left|\frac{K_i}{K_w}\right|^2 \left(\frac{6}{\pi\rho_i}\right)^2 a_m^2, \quad (3)$$

$$b_z = 2b_m - 6, \quad (4)$$

where ρ_i is the density of solid ice, K_i is the complex dielectric factor for ice, and K_w is the complex dielectric factor for liquid water. We have compared this approach to radar backscatter cross sections reported by Liu (2008) that were calculated with the discrete dipole approximation and find reasonable agreement out to particle sizes of 1 mm.

Substituting Eq. (1) into Eq. (2), and integrating over D, Z_e can be expressed as

$$Z_e = \sum_{x=l,s} Z_{e,x} = \sum_{x=l,s} A_x e a_{Z,x} D_{g,x}^{b_{z,x}+7} \Gamma(\alpha_x + b_{Z,x} + 7), \quad (5)$$

where Γ stands for the gamma function $\Gamma(x) = \int_0^\infty t^{x-1} e^{-t} dt$, and e is Euler's number exp(1).

For the Doppler velocity, we use the development of DM06 and assume that the quiet air Doppler velocity is the difference between the observed Doppler velocity and the mean vertical air motion ($V_{\text{dq}} = V_d - w$) and write

$$V_{\text{dq}} = \frac{1}{Z_e} \int_0^\infty V(D) a_z N(D) D^{b_z+6}\, dD, \quad (6)$$

where $V(D)$, the fall speed of an ice crystal of maximum dimension D, is parameterized by a power-law expression as

$$V(D) = a_v D^{b_v}. \quad (7)$$

Using the coefficients of Mitchell (1996), the empirical coefficient a_v and exponent b_v depend on the air density and the particle habit assumptions that determine the crystal mass and cross-sectional area in terms of maximum dimension:

$$a_v = a\nu \left(\frac{2a_m g}{\rho_a \nu^2 a_a}\right)^b, \quad (8)$$

$$b_v = b(b_m + 2 - b_a) - 1, \quad (9)$$

where ν is the kinematic viscosity, ρ_a is the air density, a_a and b_a are the coefficient and exponent of an area–dimensional power-law relationship, and a and b are the

prefactor and exponent of a Reynolds number–Best number power-law relationship described in Mitchell (1996).

Substituting Eq. (1) into Eq. (6) and integrating over all particle sizes, the quiet air Doppler velocity V_{dq} can be expressed analytically as

$$V_{\mathrm{dq}} = \sum_{x=l,s} V_{\mathrm{dq},x} = \sum_{x=l,s} a_{v,x} D_{g,x}^{b_{v,x}} \frac{\Gamma(\alpha_x + b_{z,x} + b_{v,x} + 7)}{\Gamma(\alpha_x + b_{z,x} + 7)}. \tag{10}$$

Thus, once the coefficient a_v and exponent b_v are calculated according to Eqs. (8) and (9), V_{dq} can be expressed as a function of the size distribution parameters only.

The visible extinction coefficient can be expressed as a function of the particle size distribution:

$$\beta_{\mathrm{ext}} = \int_0^\infty Q_{\mathrm{ext}}(D) A(D) N(D)\, dD, \tag{11}$$

where Q_{ext} is the extinction efficiency, and $A(D)$ is the particle cross-sectional area as a function of particle size D:

$$A(D) = a_a D^{b_a}. \tag{12}$$

In this study, β_{ext} is derived from Raman lidar measurements using the formalism provided by Ansman et al. (1990) and recently implemented by Comstock et al. (2008).

Substituting Eqs. (1) and (12) into Eq. (11), assuming that $Q_{\mathrm{ext}} = 2$ and integrating over all sizes, results in

$$\beta_{\mathrm{ext}} = \sum_{x=l,x} \beta_{\mathrm{ext},x} = \sum_{x=l,x} 2A_x e a_{a,x} D_{g,x}^{b_{a,x}+1} \Gamma(\alpha_x + b_{a,x} + 1). \tag{13}$$

We note that parameter α_x affects the breadth of the distribution modes. However, from our sensitivity test, the breadth of the resultant distribution can be adjusted by changing the other parameters A_x and $D_{g,x}$. Hereafter, α_x is fixed to an integer value of one for both the small and large modes.

To constitute a covariance matrix to retrieve the uncertainties of PSD parameters, a fourth forward model equation is proposed for convenience by stating that at some size D_q, the ratio of the number concentrations of the two PSD modes is unity:

$$R = \frac{N_s(D_q)}{N_l(D_q)} = 1. \tag{14}$$

In the inversion of the forward model equations, D_q is iteratively adjusted within a specified range to find a value of D_q that best fits the radar and lidar measurements.

The bulk microphysical properties such as IWC, mass-weighted mean particle size D_m, and N_t can be derived from the particle size distribution parameters using a mass–dimensional power-law relationship as before, and integrating over all particle sizes:

$$\mathrm{IWC} = \int_0^\infty a_m D^{b_m} N(D)\, dD = \sum_{x=l,s} A_x a_{m,x} e D_{g,x}^{b_{m,x}+1} \Gamma(b_{m,x} + \alpha_x + 1). \tag{15}$$

Similarly, D_m can be expressed as

$$D_m = \frac{\int_0^\infty a_m D^{b_m+1} N(D)\, dD}{a_m D^{b_m} N(D)\, dD} = \sum_{x=l,s} D_{g,x} \frac{\Gamma(\alpha_x + b_{m,x} + 2)}{\Gamma(\alpha_x + b_{m,x} + 1)} \tag{16}$$

and N_t as

$$N_t = \int_0^\infty N(D)\, dD = \sum_{x=l,x} A_x e D_{g,x} \Gamma(\alpha_x + 1). \tag{17}$$

b. Algorithm implementation

The radar and lidar measurements are described using a PSD function with four variables that include eight empirically specified parameters in four forward model equations. If we use vector $\mathbf{d} = (Z_e, V_{\mathrm{dq}}, \beta_{\mathrm{ext}})$ to represent the radar and lidar measurements, vector $\mathbf{x} = (A_s, D_{\mathrm{gs}}, A_l, D_{\mathrm{gl}})$ to stand for PSD parameters that need to be retrieved, vector $\mathbf{m} = (a_{\mathrm{ms}}, b_{\mathrm{ms}}, a_{\mathrm{ml}}, b_{\mathrm{ml}}, a_{\mathrm{as}}, b_{\mathrm{as}}, a_{\mathrm{al}}, b_{\mathrm{al}})$ to stand for the empirically derived model parameters, and F to represent the forward model equations, the problem can be symbolically expressed as $\mathbf{d} = F(\mathbf{x}, \mathbf{m})$.

Our objective is to estimate the PSD parameters by solving the inverse problem expressed as $\mathbf{x} = F^{-1}(\mathbf{d}, \mathbf{m})$. Since only three measurements are available to retrieve four unknowns, this inverse problem is ill posed and a particular solution for $\mathbf{x}$ may not be unique. Therefore, regularization methods must be used in the retrieval algorithm (Zhdanov 2002).

One way to obtain an optimal estimate of $\mathbf{x}$ is to use a priori information in the regularization and maximize the a posteriori probability $P(\mathbf{x}|\mathbf{d})$, which is the conditional probability of $\mathbf{x}$ given $\mathbf{d}$. Based on Bayes' theorem and a Gaussian probability density function (PDF) assumption, the cost function to be minimized in the optimization is derived in Zhdanov (2002) and Rodgers (2000) as

$$f(\mathbf{x}) = [\mathbf{d} - F(\mathbf{x}, \mathbf{m})]^{\mathrm{T}} \mathbf{S}_d [\mathbf{d} - F(\mathbf{x}, \mathbf{m})] + (\mathbf{x} - \mathbf{x}_a)^{\mathrm{T}} \mathbf{S}_a (\mathbf{x} - \mathbf{x}_a), \quad (18)$$

where $\mathbf{x}_a$ is the a priori of the vector $\mathbf{x}$, $\mathbf{S}_a$ is the covariance matrix of $\mathbf{x}_a$, and $\mathbf{S}_d$ is the covariance matrix of the measurement vector $\mathbf{d}$.

To find the vector $\mathbf{x}$ that minimizes Eq. (18), the first derivative of the cost function is first set to zero and then solved for $\mathbf{x}$:

$$\mathbf{x} = \mathbf{x}_a + \mathbf{S}_d \mathbf{K}_x^{\mathrm{T}} \mathbf{S}_d^{-1} [\mathbf{d} - F(\mathbf{x}, \mathbf{m})], \quad (19)$$

where $\mathbf{K}_x$ is the Jacobian matrix that represents the sensitivity of the forward model to the PSD parameters being retrieved. This equation can be solved numerically using the Gauss–Newton method:

$$\mathbf{x}_{i+1} = \mathbf{x}_i + (\mathbf{S}_a^{-1} + \mathbf{K}_x^{\mathrm{T}} \mathbf{S}_d^{-1} \mathbf{K}_x)^{-1} \times \{\mathbf{K}_x^{\mathrm{T}} \mathbf{S}_d^{-1} [\mathbf{d} - F(\mathbf{x}_i, \mathbf{m})] - \mathbf{S}_a^{-1} (\mathbf{x}_i - \mathbf{x}_a)\}. \quad (20)$$

Like any numerical method, the Gauss–Newton method may converge to a local minimum instead of the global minimum because of the choice of initial guesses. Thus, in the implementation of the algorithm we set the initial guesses of PSD parameters to a range of values, perform the Gauss–Newton method for each initial guess, and choose the result with the minimum difference between lidar–radar inputs and lidar–radar estimates as the final result.

We find that the uncertainties in model parameters and measurement errors dominate the error budget. The total measurement error includes systematic error due to instrument calibration and measurement noise, which is assumed to be random and unbiased. For radar reflectivity, based on a known uncertainty in the Millimeter Cloud Radar (MMCR) calibration of approximately 1–2 dBZ (Clothiaux et al. 1999), a 25% error is applied to the radar reflectivity. The terminal fall velocity V_{dq} is from the retrieval of DM06; the retrieval error is approximately 30%. The measurement error for the lidar extinction is derived during the retrieval of that quantity from the Raman lidar measurements (Comstock et al. 2008) and depends on the signal to noise ratio, laser power fluctuations, and solar noise. The measurement errors are assumed to be random and uncorrelated in the error covariance matrix $\mathbf{S}_x$.

Eight model parameters are used in the forward model equations, which are mass–dimensional power-law coefficients a_{ms}, a_{ml}, b_{ms}, and b_{ml}, and area–dimensional power-law relationship coefficients a_{as}, a_{al}, b_{as}, and b_{al}. The values of these model parameters are primarily dependent on particle habits, and substantial variations exist in these parameters for different particle habits. The effects of the habit uncertainties are discussed in more detail below.

TABLE 1. Sensitivity of retrieved PSD parameters to uncertainty in empirical relationships (5% $\mathbf{S}_\varepsilon$, 100% $\mathbf{S}_a$).

	Retrieval errors (%)						
$\mathbf{S}_m$ (%)	A_s	D_{gs}	A_l	D_{gl}	IWC	D_m	N_t
5	72.3	18.8	60.2	19.9	77.5	16.6	67.9
10	87.0	22.4	78.8	30.9	116.3	25.4	83.9
50	97.6	25.5	95.4	73.4	217.3	60.1	92.1
100	98.3	26.5	97.3	90.0	233.7	72.4	92.9

After the measurement covariance matrix $\mathbf{S}_\varepsilon$ and the model parameter covariance matrix $\mathbf{S}_m$ are quantified, the retrieval $\mathbf{S}_x$ can be derived as

$$\mathbf{S}_x = (\mathbf{K}_x^T \mathbf{S}_d^{-1} \mathbf{K}_x + \mathbf{S}_a^{-1})^{-1}. \quad (21)$$

In Eq. (21), $\mathbf{S}_d$ is written as

$$\mathbf{S}_d = \mathbf{S}_\varepsilon + \mathbf{K}_m \mathbf{S}_m \mathbf{K}_m^{\mathrm{T}}, \quad (22)$$

where $\mathbf{K}_m$ is the Jacobian matrix representing the sensitivity of the forward model to the model parameters.

The retrieval error, therefore, depends on measurement errors and uncertainties in the model parameters. To quantify the relative magnitude of these error and uncertainty contributions, a sensitivity test of the retrieval algorithm error to the measurement errors and the empirical relationship uncertainties is performed. The sensitivity of the retrieval errors to the model parameter uncertainties is tested by varying the model parameter uncertainties and fixing the measurement errors to small values of 5%. Using typical input quantities—for example, $\mathbf{d} = (-30\ \mathrm{dB}Z, 45\ \mathrm{cm\ s^{-1}}, 0.15\ \mathrm{km^{-1}})$—as the input to the algorithm, the retrieval errors of four PSD parameters are given by Eq. (21), and the uncertainty in IWC, D_m, and N_t is calculated and reported in Table 1. We find that as the model parameter uncertainty increases from 5% to 100%, the uncertainty in the geophysical quantities of most interest grows dramatically. By fixing the model parameter covariance to 5% and varying the measurement errors, the retrieval sensitivity to measurement errors is also tested (Table 2). We find that the retrieval errors are significantly more sensitive to uncertainties in empirical parameters than to reasonable uncertainties in measurements. This finding is consistent with results reported in Zhang and Mace (2006) and DM06.

TABLE 2. Sensitivity of retrieved PSD parameters to uncertainty in measurements (5% $\mathbf{S}_m$, 100% $\mathbf{S}_a$).

	Retrieval errors (%)						
$\mathbf{S}_e$ (%)	A_s	D_{gs}	A_l	D_{gl}	IWC	D_m	N_t
5	72.3	18.8	60.2	19.9	77.5	16.6	67.9
10	76.9	20.1	60.9	20.1	78.2	16.7	72.5
50	93.1	23.6	75.4	22.6	94.7	18.2	86.6
100	96.2	24.4	87.3	27.3	112.8	21.9	89.7

3. Case studies

In situ measurements including the particle concentration and the IWC collected by airborne instruments on board the University of North Dakota (UND) Citation during the 2000 Cloud intensive observing period (IOP) are used to compare with retrievals from the ground-based remote sensing data using the algorithm described in the previous section. Because of time and space differences between the aircraft in situ measurements and the ground-based remote sensing data, comparing quantities measured by aircraft in situ probes and ground-based remote sensors is challenging (e.g., Matrosov et al. 1998; Mace et al. 2002). This difficulty is exacerbated by the Raman lidar integration period of 10 min because of the need to reduce noise caused by the solar background during daytime (Comstock et al. 2008). Assuming that the cirrus clouds are moving at speeds of 30 m s^{-1}, the horizontal spatial dimension of the Raman lidar can be as large as 18 km. For the aircraft in situ measurements, assuming the aircraft is flying at horizontal speed of 100 m s^{-1}, a 5-s average would provide a horizontal spatial resolution of 500 m. Because of this mismatch in scale, a statistical approach must be used to make reasonable comparisons of data collected from the two platforms. The simple approach we adopt relies on the fact that the aircraft flew horizontal legs along the ambient wind direction. By assuming negligible changes in cloud properties between the time of measurement by the aircraft and when the remote sensors measured the volume, in situ measurements sampled at locations up to 20 km upstream and downstream from the SGP site are used in the comparison. We consider each 5-s averaged aircraft measurement to constitute a sample of the cloud properties and, by translating that measurement in time to the measurement period at the ground site, we estimate in which time–height remote sensing data bin an in situ measurement can be most reasonably placed. In essence, in situ measurements collected upstream of the ground site are moved forward in time at the geometrical height of the measurement and in situ measurements collected downstream of the ground site are moved backward in time. The aggregated in situ data in each remote sensing data bin are then compared with the remote sensing retrieval. The statistics of the seven horizontal legs flown by the UND Citation on 9 March 2000, illustrated against the MMCR height–time cross section in Fig. 1d, are compared to the algorithm results and summarized in Table 3.

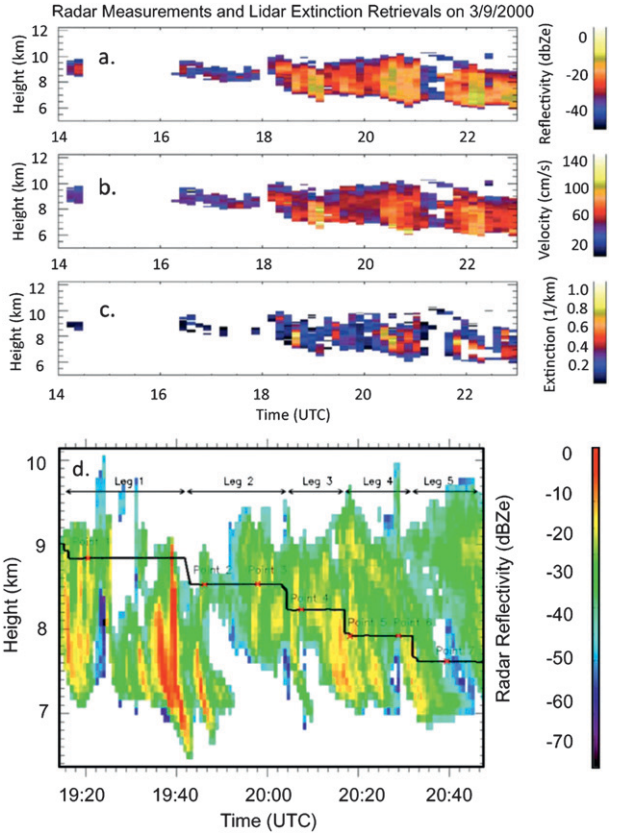

FIG. 1. The (a) MMCR radar reflectivity, (b) Doppler velocity, and (c) Raman lidar-derived extinction height–time cross section on 9 Mar 2000 averaged to the 10-min time resolution of the Raman lidar. In (d), the aircraft track is overlaid on the radar reflectivity height–time cross section during the time of the flight. The black solid line shows the flight path of the University of North Dakota Citation and the red crosses denote the nominal times of the seven retrievals to which the in situ data are compared.

Figure 1 illustrates the ground-based remote sensing data collected on 9 March 2000 that are used as input to the algorithm and used in the case study. A careful evaluation of this data shows regions of the layer where extinction is high while the radar reflectivity and Doppler velocity are low, suggesting that small particles and potential PSD bimodality are present. Other regions in the cirrus layer, mostly near layer base, show regions with smaller extinction and larger reflectivity and Doppler velocity suggesting the presence of only larger particles that are sedimenting from above. Because of the 10-min time resolution of the Raman lidar, there are only seven

TABLE 3. The mean and standard deviation of IWC in situ data and IWC retrieval. The points refer to the 5-min averages centered on the point listed in Fig. 2.

	In situ measurements (mg m^{-3})			Retrievals (mg m^{-3})	
	Mean	Normalized std dev	Sample quantity	Solution	Relative uncertainty (%)
1	4.38	3.69	3	6.01	90
2	3.31	2.77	29	2.33	80
3	11.91	6.89	27	5.24	93
4	22.34	12.90	17	5.64	90
5	11.34	9.27	29	5.35	90
6	8.29	6.82	24	2.32	88
7	7.29	7.91	38	1.62	56

retrieval results available for comparison with the aircraft data during the five horizontal legs, which are shown as the red crosses in Fig. 1d. However, only the second and the third PSD retrievals on the second horizontal leg suggest strong bimodality, and the comparisons with in situ measurements are shown in Fig. 2.

In Fig. 2, the estimated uncertainties of PSD retrievals due to uncertainties in radar and lidar data and the empirically derived model parameters are shown by the heavy solid green curves drawn on either side of the optimal PSD estimate shown by the smooth solid black curves. Since bullet rosettes are the predominant particle habits on 9 March 2000 as found by Heymsfield et al. (2002), the mass– and area–dimensional parameters for five branch bullet rosettes in Mitchell (1996) are used in the algorithm. The uncertainties of mass, area, and velocity resulting from these model parameters are assumed to be 20% (Mitchell 1996; Heymsfield et al. 2002), and the uncertainties for Z_e, V_{dq}, and β_{ext} are assumed to be 25%, 30%, and 20%, respectively.

The thin blue curves in Fig. 2 show all 5-s averaged in situ measurements that are associated with a particular vertical and temporal retrieval interval and the red line is the average of all the 5-s averages. We find that for large particles, most PSD in situ measurements from the 2DC fall inside the retrieval uncertainty envelope, and the PSDs averaged from the 5-s data agree reasonably well with the large-mode PSD retrievals. However, for small particles (<50 μm maximum dimension), the averaged concentration from the FSSP is about 10 times larger than that of the retrieved small-mode concentration, and all in situ PSD measurements from the FSSP collected during the averaging interval are well outside the retrieval uncertainty envelope.

Because the Raman lidar extinction primarily determines the properties of the small particle mode in the retrieval algorithm, we adjusted the extinction used as input to the retrieval algorithm to larger values until we approximately matched the in situ measurements of small particles. We found that an artificial increase in the input extinction by a factor of 5 approximately reproduced the in situ PSDs reported by the FSSP. In other words, for point 3, as an example, an increase in extinction from 0.35 to 1.75 km^{-1} is necessary to reproduce the in situ measurements. The optical depth derived from multifilter rotating shadow band radiometer derived using the technique of Min and Harrison (1996) gave an average optical depth during this 10-min period of 0.8 while the Raman lidar optical depth in the cirrus was approximately 0.85. Given that the cirrus layer was more than 2 km deep during this period, there appears to be no reasonable interpretation of the remote sensing data that

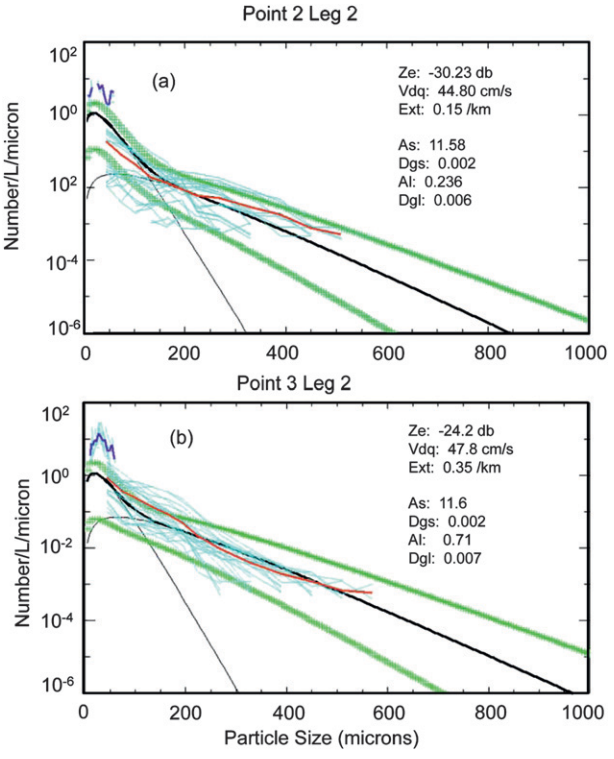

FIG. 2. Comparison of the retrieved PSDs and the PSD in situ measurements. (a) Point 2 in leg 2 at approximately 1946 UTC. (b) Point 3 in leg 2 at 1955 UTC.

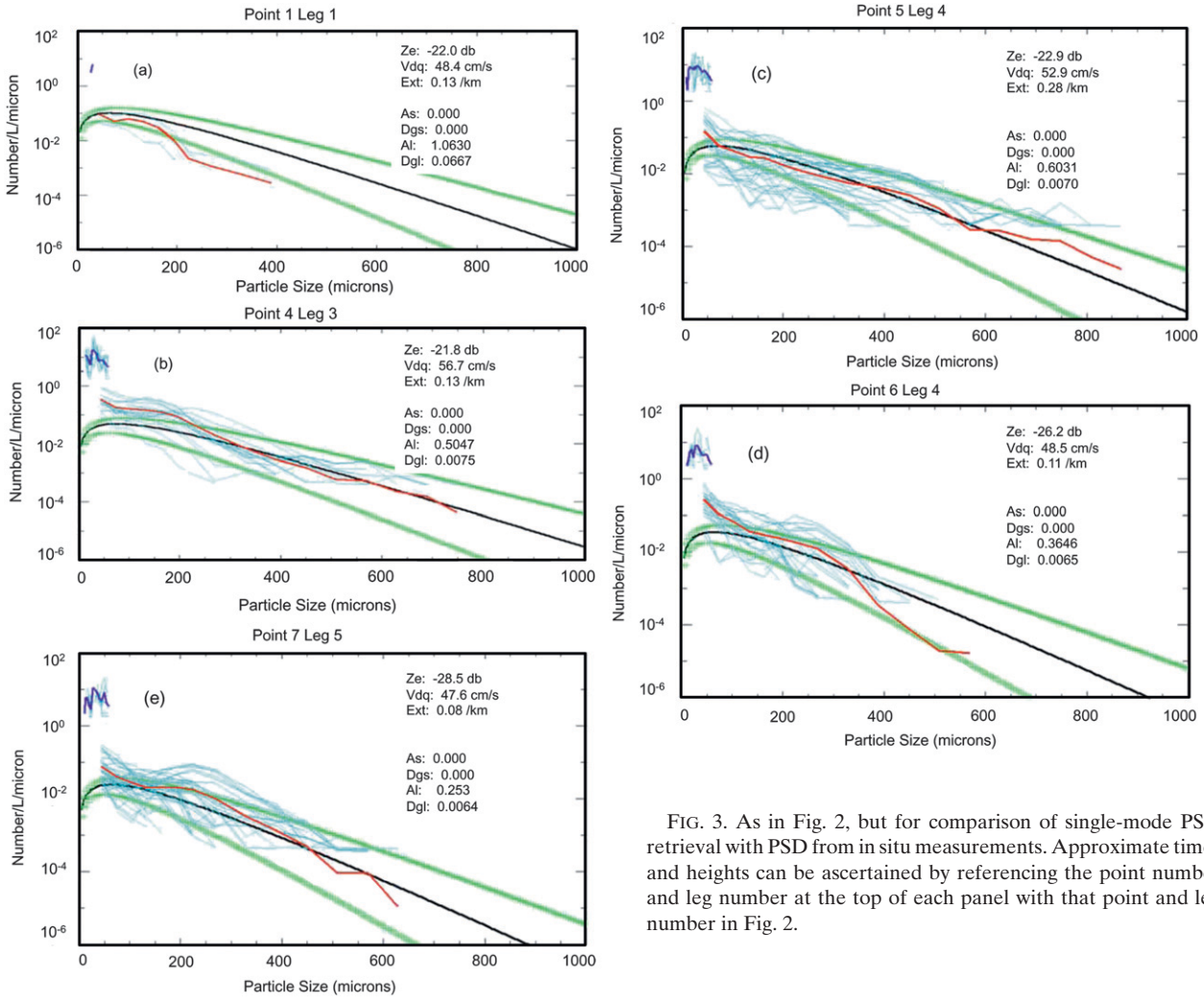

FIG. 3. As in Fig. 2, but for comparison of single-mode PSD retrieval with PSD from in situ measurements. Approximate times and heights can be ascertained by referencing the point number and leg number at the top of each panel with that point and leg number in Fig. 2.

can rectify the differences between the in situ small particle measurements and the retrieved cloud microphysical and radiative properties.

The other five comparisons of PSD during the horizontal flight legs are shown in Fig. 3. In these cases, the remote sensing data suggest a single-mode PSD because the extinction derived from an assumed single-mode PSD (using the radar data alone) is greater than or equal to the Raman lidar extinction. For these PSD comparisons, the PSD retrievals also agree well with the averaged 2DC in situ measurements, and most 2DC in situ measurements used in the average fall inside the uncertainty envelope of the PSD retrievals.

4. Cirrus statistics

The retrieval algorithm described in section 2 is applied to 313 h of cirrus (33 641 10-min averages) observed at the Atmospheric Radiation Measurement Program (ARM) Southern Great Plains (SGP) site during 2000, and frequency distributions (PDFs) of IWC, effective radius r_e, and N_t are derived from these results. We examine the vertical structures of these statistics and derive the properties of PSD bimodality as a function of depth within the cirrus layers for different temperature regimes.

a. *Microphysical properties*

IWC and N_t are calculated from the PSD retrievals using Eqs. (15) and (17). For r_e, we note that various definitions have been used in the literature (McFarquhar and Heymsfield 1998). Here, we use a universal definition provided by Mitchell (2002), which is written as

$$r_e = \frac{3\mathrm{IWC}}{4\rho_i P}, \tag{23}$$

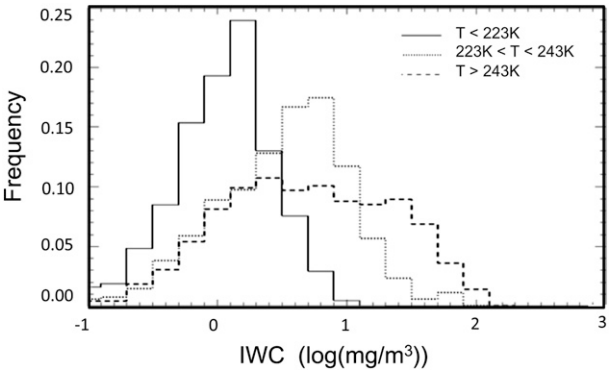

FIG. 4. Frequency distribution of IWC derived from 313 h of cloud property retrievals using the bimodal algorithm. The distributions are shown as a function of the layer-mean temperature shown in the legend.

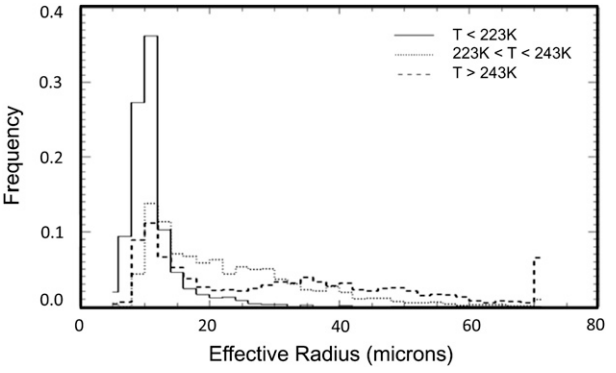

FIG. 5. As in Fig. 4, but for the retrieved effective radius of the retrieved particle size distributions.

where P is the projected cross section and ρ_i is the density of ice.

Figures 4, 5, and 6 illustrate the PDFs (summarized in Table 4) of IWC, r_e, and N_t, respectively, for three temperature regimes that represent what we define as warm ($T > 243$ K), cold ($T < 223$ K), and intermediate cirrus layers. As expected, a clear dependence on temperature (e.g., Heymsfield and Platt 1984) is seen in all three properties. The coldest regime has the lowest IWC mean value, about 1.61 mg m^{-3} with a standard deviation of 2.69 mg m^{-3}. The warmest regime has the highest mean value, which is 12.60 mg m^{-3} with a standard deviation of 17.07 mg m^{-3}, and the intermediate cirrus has a mean IWC of 6.09 mg m^{-3} (standard deviation of 10.59 mg m^{-3}).

It is interesting to note that the normalized standard deviations of IWC are 1.7, 1.7, and 1.3 for the coldest, intermediate, and warmest cirrus, respectively. The distributions of IWC are approximately log-normally distributed with the cold cirrus having a very peaked and narrow PDF with a maximum value of almost 25% in the range between 1.25 and 2.0 mg m^{-3}. The middle-temperature cirrus has a relatively lower maximum frequency (about 17%) at a larger IWC (about 8.0 mg m^{-3}), and for the warmest cirrus the PDF is flat and ranges from 1.25 to 31.6 mg m^{-3}. In essence, the minimum values are not really a function of temperature and are more likely a function of the sensitivity threshold of the MMCR while the breadth of the PDF extends log-normally to higher values as the temperature increases.

The PDFs of r_e also demonstrate a strong dependence on temperature with highly skewed distributions. One significant feature of the r_e PDF shown in Fig. 5 is the high peak at about 10 μm for the PDF of the coldest cirrus. The coldest cirrus r_e PDF reaches a maximum of about 35%, which is more than twice the maximum of the warmest and intermediate cirrus PDFs, and then it quickly decreases to a frequency near zero at 30 μm. More than 80% of the PDF area falls below 20 μm, which suggests that for the coldest cirrus, most effective radii are below 20 μm. While the r_e PDF maxima of intermediate and warm cirrus are smaller, they both have a much wider PDF widths, extending from 5 μm to more than 70 μm. More than 50% of the PDF area is above 20 μm for the warm and intermediate temperature ranges.

With regard to the mean values, the coldest cirrus has the smallest mean r_e, at about 12 μm with a standard deviation of 6.9 μm; the warmest cirrus has the largest mean value, about 31 μm with a standard deviation of about 21 μm; and the mean r_e for intermediate cirrus is about 23 μm with a standard deviation of 14 μm. The mean values of the effective radius retrievals are generally smaller than that of previous studies (e.g., Wang and Sassen 2002); however, they are consistent with the results reported by Donovan (2003), who also assumed a bimodal PSD in his lidar–radar retrieval algorithm. These values of r_e are also reasonably consistent with the

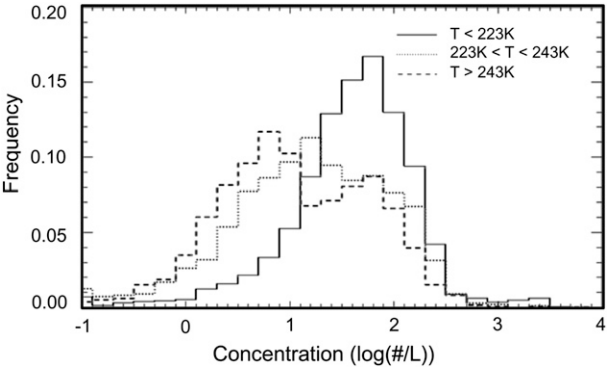

FIG. 6. As in Fig. 4, but the total number concentration of the retrieved particle size distributions.

TABLE 4. Means and standard deviations of retrieved IWC, effective radius, and total number concentration as a function of the temperature regimes (coldest $T < 223$ K; intermediate 223–243 K, and warmest $T > 243$ K) derived from the 313 h of cirrus data over SGP.

	IWC (mg m^{-3})		Effective radius (μm)		Concentration (L^{-1})	
	Mean	Std dev	Mean	Std dev	Mean	Std dev
Coldest $T < 223$ K	1.609 30	2.685 11	11.5543	6.885 49	101.023	276.526
Intermediate $223 < T < 243$ K	6.087 25	10.5858	23.2374	14.0517	57.5514	167.777
Warmest $T > 243$ K	12.6046	17.0654	30.7738	21.0104	40.1578	211.809

findings at these temperatures of Garrett (2008), who analyzed in situ data from bulk probes collected in midlatitude cirrus.

The PDFs of N_t as a function of temperatures are shown in Fig. 6. The mean N_t for the cold cirrus is about 101 L^{-1} (0.10 cm^{-3}) with a standard deviation of 277 L^{-1}, while for intermediate and warm cirrus, N_t is 58 L^{-1} (standard deviation of 168 L^{-1}) and 40 L^{-1} (standard deviation of 212 L^{-1}), respectively. The cold cirrus has a much larger mean N_t than the others. In terms of PDF mode, the PDF of the cold cirrus is the narrowest; 80% of its area is from about 10 to 400 L^{-1}. For the warm and intermediate cirrus, their PDF widths are wider, and there is more PDF area in the region of 1–10 L^{-1}. However, for all cirrus, the occurrence frequencies of the total number concentrations larger than 1000 L^{-1} (1 cm^{-3}) are well below 1%.

The remote sensing retrievals from the lidar–radar algorithm show unambiguously that $N_t > 1000$ L^{-1} is rare in the cirrus clouds examined here. This finding is not consistent with in situ measurements that are not carefully filtered for shattering artifacts. In such studies, the average particle concentration in midlatitude cirrus is reported to be on the order of 1000 L^{-1} (1 cm^{-3}) (Lawson et al. 2006) or higher [>5 cm^{-3} reported by Gayet et al. (2002)]. The presence of shattering artifacts is likely the prime reason for this large discrepancy (McFarquhar et al. 2007; Jensen et al. 2009). Regardless of the reason, we can conclusively state that such average concentrations as derived from aircraft data (>~1000 L^{-1} and larger) are not consistent with any reasonable interpretation of the Raman lidar and Doppler radar data collected at the ARM SGP site.

Next, we examine the vertical structure of IWC, r_e, and N_t within depth-normalized layers that are segregated as a function of temperature as before (Figs. 7–9). The IWC and r_e both tend to increase from layer top downward where, for the intermediate and warm cirrus, both quantities tend to decrease in the lower 20% of the layer. This structure suggests that sublimation processes dominate the lower 20% or so of these layers as the ice crystals sediment into drier layers. The slow time scale for sublimation and the rather rapid sedimentation velocity of mature cirrus particles cause this sublimation zone to be quite broad (Heymsfield and Donner 1990). There is a very distinct vertical weighting of the total ice mass and particle size that is a strong function of temperature. For the coldest layers IWC and r_e do not vary substantially from radar layer top and layer base. There is a slight increase near layer center for both IWC and r_e, but this vertical variation in structure in the cold layers is not nearly so pronounced as in the intermediate and warmer cirrus.

Note that N_t behaves differently from IWC and r_e. The warmer temperature regime shows a steady decrease in total number from top to the lower portion of the layer consistent with aggregation processes (Liu et al. 2003; Westbrook et al. 2007). Concentrations seem to be similar at layer top for the three temperature regimes. The N_t values of the warm cirrus then decrease most rapidly as r_e increases most rapidly. It is likely that since IWC increases also, the increase in r_e is not due solely to aggregation but also to depositional processes. It is interesting to note that N_t increases in the lower portion of the layer where r_e and IWC are also increasing. This finding is consistent with the modeling results of Liu et al. (2003),

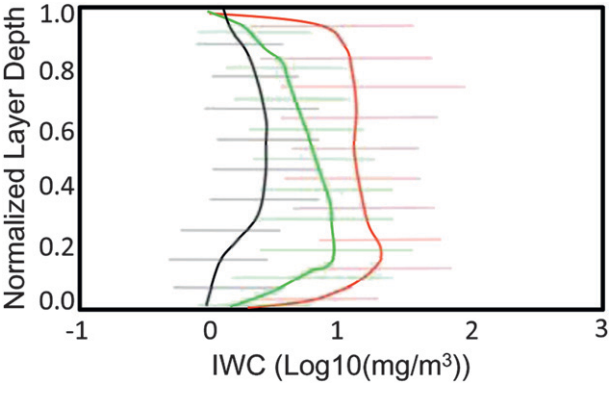

FIG. 7. Vertical profiles of IWC from the retrieved particle size distributions. Shown are the means and standard deviations as a function of normalized layer depth with a vertical coordinate of 1.0 depicting cloud top and 0 depicting cloud base. The red, green, and black curves correspond respectively to layer-mean temperature ranges of >243, 243–223, and <223 K.

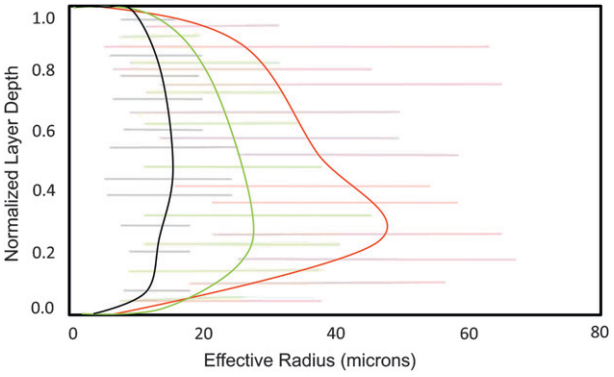

FIG. 8. As in Fig. 7, but the effective radius is shown.

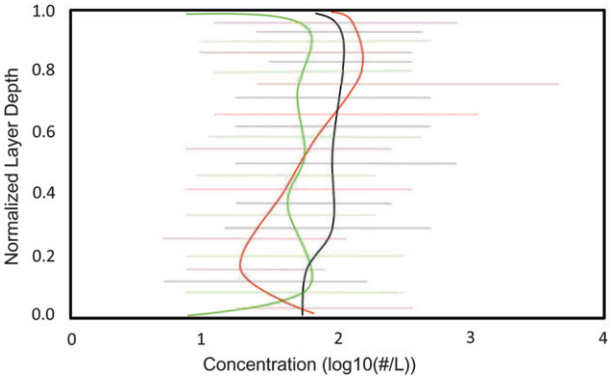

FIG. 9. As in Fig. 7, but the total number concentration is shown.

who find that ice crystals tend to collect in the lower portion of the cirrus layer as sublimating crystals fall less rapidly while larger crystals from above enter this zone.

b. PSD bimodality

The existence of bimodality in cirrus PSDs suggests the occurrence of certain microphysical processes such as secondary nucleation of ice crystals within cirrus layers (Comstock et al. 2008). The presence of significant bimodality also has implications for cirrus cloud property retrievals from ground-based and space-based sensors. We emphasize the phrase "significant bimodality" because quite often the algorithm used in this study diagnoses a PSD that utilizes both gamma functions to best represent the data. However, in many cases a unimodal description of the PSD would be sufficient, within some specified degree of uncertainty, to describe the PSD moments that are most relevant to the integrated physical quantities such as IWC, N_t, and r_e. Previous studies such as Mace et al. (2002) used aircraft in situ data to study the frequency of occurrence of bimodal size distributions in cirrus; however, an examination of bimodality has not been applied to a large remote sensing dataset.

The approach we take to quantify the frequency of bimodality is to fit the retrieved PSD by a unimodal distribution (single-moment PSD) and then to use the misfit between the retrieved PSD and the fitted single-moment PSD to ascertain the degree of bimodality of the PSD. A modified gamma function with three degrees of freedom is used as the single-moment PSD fitting function. The difference of the second, third, and fifth moments of the retrieved PSD and the fitted single-moment PSD is used as the cost function, which is expressed as

$$f = \sqrt{\sum_{x=2,3,5} \left| \frac{\mu_x' - \mu_x}{\mu_x} \right|^2}, \qquad (24)$$

where μ_x' represent moments of the fitted single-moment PSD and μ_x are moments of the retrieved PSD. Because the second, third, and fifth moments approximately correspond to β_{ext}, IWC, and Z_e respectively [b_z in Eq. (4) is order 1], the difference between the retrieved PSD and the fitted single-moment PSD can be measured by these quantities with actual physical meanings. We note that other moments of the PSD can be used in Eq. (24); however, we find little difference in the results so long as PSD moments that approximately represent the small and large PSD modes are used.

To identify an optimal single-mode fit, a commonly used nonlinear optimization algorithm (Nelder and Mead 1965) is used. Finally, a threshold value for the misfit must be specified to identify significantly bimodal PSDs from what could be approximated as single-mode PSDs or weakly bimodal PSDs. Four example PSDs are shown in Fig. 10.

In Fig. 10a, the magnitude of the small-mode PSD is insignificant and the misfit between the optimal gamma function and the bimodal PSD is only 1%. The misfit of the second PSD example increases to 10%, and the resultant PSD shows a distinct discontinuity. However, while the bimodality is more significant, it is unlikely that the differences in bulk properties would be identifiable above measurement uncertainties. In Figs. 10c and 10d, the PSD retrieval shows stronger bimodality with the misfits at 20% and 30%, respectively. From these and other examples that we have studied, 30% is chosen to be a proper threshold to distinguish strongly bimodal PSDs from unimodal or weakly bimodal PSDs. This value of misfit is approximately the degree of uncertainty that one would expect in retrieving the PSD moments from either remote sensing data or from in situ data and is therefore an appropriate threshold metric for our purposes.

Using the 313 h of 10-min average retrievals, the histogram of the bimodality frequency (the ratio of the

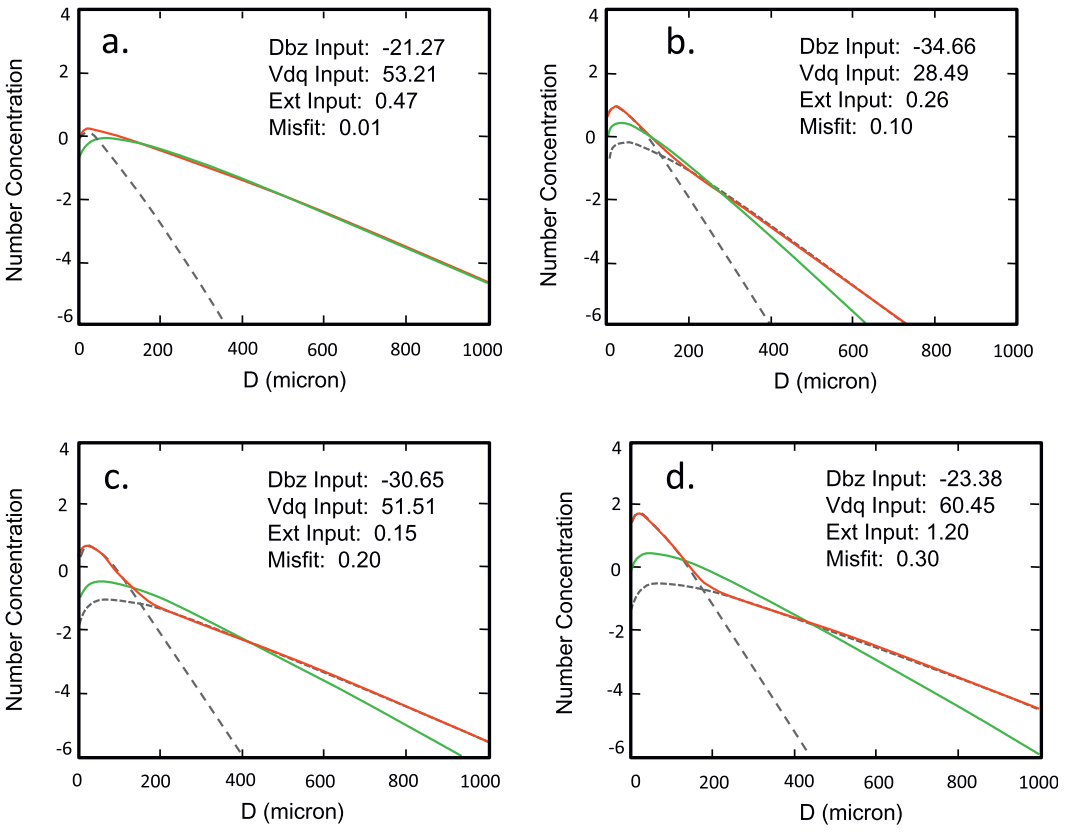

FIG. 10. Examples of PSD retrieval and PSD misfit of (a) 1, (b) 10, (c) 20, and (d) 30%. The observable quantities that produce the retrievals are shown in the inset. In each figure the dotted curves indicate the small and large PSD modes, the red curve shows the resultant PSD (the sum of the small and large modes), and the green curve shows the best-fit single-mode modified gamma function.

number of strongly bimodal PSD occurrences to the total number of PSD occurrences in a given radar reflectivity and temperature bin) in terms of radar reflectivity and temperature is shown in Fig. 11. Generally, we find that the occurrence of bimodality increases from cold to warm temperatures and from high to low Z_e. The bimodality frequencies for cirrus with very small radar reflectivities (less than -35 dBZ_e) at very low temperatures (lower than 230 K) are generally below 25%. As the temperature increases, the bimodality frequency also increases. However, when radar reflectivity is above -15 dBZ_e, the bimodality frequency is generally less than 20% regardless of the temperature. A bimodality occurrence frequency of more than 40% occurs when the temperature is above 240 K and radar reflectivity is below -15 dBZ. When the temperature is less than 240 K, the bimodality frequency is generally less than 30%. We note a rather sudden shift in the frequency of significant bimodality at temperatures near the homogeneous nucleation threshold of 230 K and radar reflectivities in the -30 dBZ_e range where the frequency of occurrence changes by a factor of 2 as this boundary is crossed.

Segregating the bimodality occurrence in terms of temperature and normalized vertical profiles (Fig. 12), a distinct vertical structure emerges. For the coldest cirrus, the bimodality frequencies are below 20%, and the profile is rather invariant within the layer. However, for the warmest cirrus (and to a lesser extent the intermediate cirrus), the bimodality frequency drops rapidly from more than 40% near the layer top to less than 20% in the middle third of the profile. The bimodality then increases again in the lower 20% of the layer where we found the IWC and r_e decreasing and N_t increasing.

The structure in PSD bimodality in the lower 20% of the layer is consistent with the behavior of the other bulk properties and the modeling study of Liu et al. (2003) and Khvorostyanov and Curry (2008a). In this lower portion of warmer cirrus where particles have grown large because of deposition and aggregation, particles that sediment into the sublimation zone accumulate and fall progressively less rapidly as they sublimate and join the remnants of other sublimated particles in this zone.

The differences in the PSD bimodality occurrence of the warm and cold cirrus shown in Fig. 12 may be

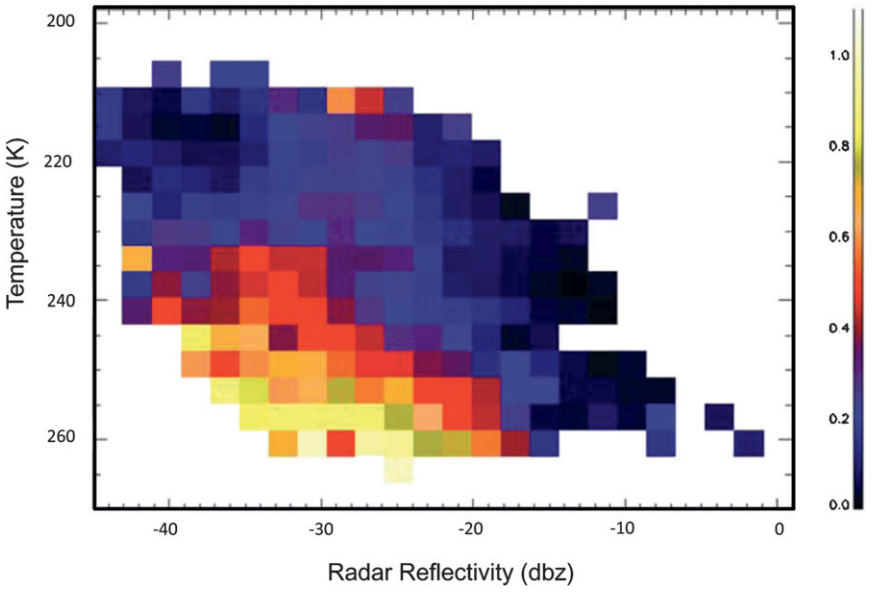

FIG. 11. The frequency of occurrence of significant bimodality as a function of the resolution volume temperature and averaged radar reflectivity in the cirrus particle size distributions retrieved from the bimodal algorithm applied to 313 h of data at the SGP site (using 30% difference between PSD retrieval and single-moment PSD fit as the threshold). The color represents the fraction of total volumes with the indicated properties that are deemed to have significant bimodality.

associated with the distinct microphysical processes that occur at their respective temperatures, as found by Comstock et al. (2008). In the warmer layers, any heterogeneous ice nuclei that are active at these temperatures could initiate small particle populations in turbulent updrafts that reach ice saturation. This contention is also supported by the shift in bimodality occurrence seen in Fig. 11 at temperatures near 230 K and reflectivities of -30 dBZ_e. Khvorostyanov and Sassen (1998b), who include both heterogeneous and homogenous nucleation mechanisms in their numerical simulations, illustrate this process in their Fig. 4 and the associated discussion in that paper. Khvorostyanov and Curry (2008a) also demonstrate that bimodal PSDs could evolve naturally without this mechanism through depositional growth and sedimentation from above. At cold temperatures these processes would be less efficient (Sassen and Dodd 1989). Turbulent updrafts that create ice supersaturation in the presence of preexisting ice crystals within the cold cirrus layer with few active ice nuclei would prohibit water saturation from being reached resulting in much rarer bimodal PSD occurrence frequencies.

5. Summary

A literal interpretation of in situ cirrus datasets collected in the last 30 years suggest that typical number concentrations in these clouds regularly exceed 1000 L^{-1} and may average as high as 5000 L^{-1} (e.g., Gayet et al. 2002). The aircraft in situ data suggest that cirrus PSDs are dominated by strongly bimodal particle spectra with a distinct ''cloud'' mode of particles smaller than 50 μm coexisting with a precipitation mode of particles that are several hundred microns in maximum dimension (Ivanova et al. 2001). Recent critical examinations of aircraft measurements suggest that data from certain probes such as the FSSP may be contaminated by ice crystal shattering on probe inlets (McFarquhar et al. 2007; Heymsfield 2007; Jensen et al. 2009). However, while these studies used newer probe data with more sophisticated processing techniques, the use of in situ data to

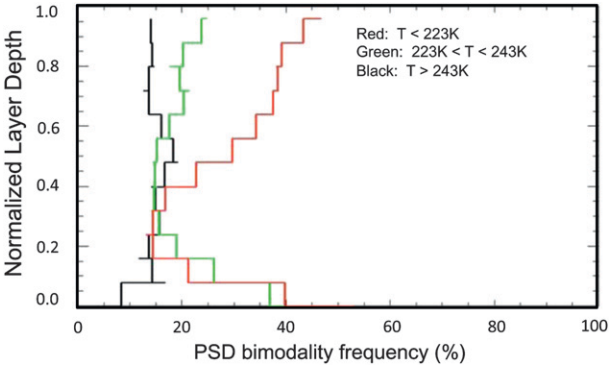

FIG. 12. Vertical profiles of the frequency of occurrence of significant bimodality as a function of layer-mean temperature derived from 313 h of cirrus over the SGP site. The vertical coordinate is as in Fig. 7.

address this problem raises questions about possible uncertainties associated with the data processing techniques and measurement approaches. A proper interpretation of long-term remote sensing data would provide an accurate statistical description of cirrus properties and, one hopes, help resolve this issue.

A principal characteristic of the in situ data that reports high concentrations of small crystals is that the cirrus PSDs are strongly bimodal. Therefore, any interpretation of the remote sensing data must allow for such bimodality. An algorithm that uses millimeter-wavelength Doppler radar moments and Raman lidar extinction is developed to retrieve cirrus PSDs that can be described by two independent modified gamma functions. These distribution functions when combined have the capacity to describe the strongly bimodal PSDs reported by aircraft in situ probes because the lidar extinction is more sensitive to small particles (i.e., the second moment of the PSD) and the radar reflectivity is more sensitive to large particles (fifth to sixth moment of the PSD). A set of forward model equations for radar reflectivity, Doppler velocity, and lidar extinction is developed based on the bimodal PSD and an inversion method is applied using the maximum a posteriori criterion, the Gaussian PDF assumption, and the Gauss–Newton numerical method to determine both the optimal solution and the uncertainty of that solution.

We test the capacity for the algorithm to reach an optimal estimation of the PSD parameters and find that regularization must be used because of the ill-posedness of the inverse problem. By using multiple initial guesses and the Gauss–Newton method, our algorithm is capable of converging to a global optimal solution. For retrieval uncertainties, the two most significant error sources are the uncertainties of the model parameters (the assumption of particle habit) and the measurement errors. We find, as have others, that the particle habit assumption dominates the error budget, highlighting a need for a more robust statistical database from which to specify these model parameters in remote sensing retrievals.

In situ measurements from the 2000 cloud IOP at the ARM SGP site are used to compare with the retrieval results. The PSD in situ data from the 2DC for large particles agree well with data from retrievals. For smaller particles, the number concentrations observed by the FSSP are much higher (by approximately a factor of 10) than what is derived from the remote sensing data and are well outside the retrieval uncertainties. To bring the small particle concentration retrieved from the remote sensing data into agreement with the FSSP, the Raman lidar extinction would need to be increased by a factor of 5. Since the Raman lidar-derived optical depth agrees reasonably with optical depths derived from the multifilter rotating shadow band radiometer, we conclude that the FSSP data are erroneous.

Finally, the statistics of cirrus cloud microphysical properties are derived by applying the retrieval algorithm to 313 h of 10-min averages collected over the ARM SGP site during 2000. The PDFs of the IWC, the effective radius, and the number concentration are examined for cirrus with different temperatures. We find that bimodality in the PSD is rare at cold ($T < 223$ K) temperatures but is a significant feature of many cirrus layers with 40% frequencies of occurrence in warmer ($T > 243$ K) cirrus layers. In the upper half of these warm cirrus, layers where heterogeneous nucleation events can occur in the presence of larger particles sedimenting from higher levels. This process to produce bimodality is consistent with the modeling study of Comstock et al. (2008) and with the theoretical work of Khvorostyanov and Curry (2008a,b). The bimodality of the particle size distribution is often prominent enough that an assumption of a single-mode distribution function in remote sensing retrievals would be unable to simultaneously represent the number concentration, extinction, and ice water content. We also find significant bimodality in the lower 20% of the warm cirrus that is consistent with the accumulation of large sublimating particles, as found in the modeling work of Liu et al. (2003). These findings are consistent with the conclusions of Mitchell et al. (2010), who used satellite data to infer the concentrations of small ice crystals in cirrus over the eastern tropical Pacific.

We find that the occurrence frequencies of the total number concentrations larger than 1 cm^{-3} are less than 1% of all size distributions derived using the lidar–radar algorithm described in section 2. Our finding of mean concentrations on the order of 100 L^{-1} is absolutely inconsistent by a factor of more than 10 with the high concentration of small particles from literal analyses of aircraft in situ data. Our results are consistent with the findings of McFarquhar et al. (2007), Heymsfield (2007), and Jensen et al. (2009), who conclude that particle shattering on aircraft and probe surfaces artificially enhances the concentrations of small particles in certain probes not designed to minimize their impact.

Acknowledgments. Primary funding for this work was supplied by the Environmental Science Division of the U. S. Department of Energy (Grant DE-FG0398ER62571). Data were obtained from the Atmospheric Radiation Measurements Program sponsored by the U. S. Department of Energy Office of Science, Office of Biological and Environmental Research, Environmental Science Division. We thank Stephanie Avey for assistance in creating the final set of figures.

REFERENCES

Ansman, A., M. Riebesell, and C. Weitkamp, 1990: Measurement of atmospheric aerosol extinction profiles with a Raman lidar. *Opt. Lett.,* **15,** 746–748.

Arnott, W. P., Y. Dong, J. Hallett, and M. R. Poellot, 1994: Role of small ice crystals in radiative properties of cirrus: A case study, FIRE II, November 22, 1991. *J. Geophys. Res.,* **99,** 1371–1381.

Clothiaux, E. E., and Coauthors, 1999: The Atmospheric Radiation Measurement Program cloud radars: Operational modes. *J. Atmos. Oceanic Technol.,* **16,** 819–827.

Comstock, J. M., R. F. Lin, D. O. Starr, and P. Yang, 2008: Understanding ice supersaturation, particle growth, and number concentration in cirrus clouds. *J. Geophys. Res.,* **113,** D23211, doi:10.1029/2008JD010332.

Deng, M., and G. G. Mace, 2006: Cirrus microphysical properties and air motion statistics using cloud radar Doppler moments. Part I: Algorithm description. *J. Appl. Meteor. Climatol.,* **45,** 1690–1709.

Donovan, D. P., 2003: Ice-cloud effective particle size parameterization based on combined lidar, radar reflectivity, and mean Doppler velocity measurements. *J. Geophys. Res.,* **108,** 4573, doi:10.1029/2003JD003469.

Field, P. R., R. Wood, P. R. A. Brown, P. H. Kaye, E. Hirst, R. Greenaway, and J. A. Smith, 2003: Ice particle interarrival times measured with a fast FSSP. *J. Atmos. Oceanic Technol.,* **20,** 249–261.

Garrett, T. J., 2008: Observational quantification of the optical properties of cirrus cloud. *Light Scattering Reviews,* Vol. 3, A. Kokhanovsky, Ed., Praxis, 3–26.

Gayet, J. F., and Coauthors, 2002: Quantitative measurement of the microphysical and optical properties of cirrus clouds with four different in-situ probes: Evidence of small ice crystals. *Geophys. Res. Lett.,* **29,** 2230, doi:10.1029/2001GL014342.

Heymsfield, A. J., 1972: Ice crystal terminal velocities. *J. Atmos. Sci.,* **29,** 1348–1357.

——, 2007: On measurements of small ice particles in clouds. *Geophys. Res. Lett.,* **34,** L23812, doi:10.1029/2007GL030951.

——, and C. M. R. Platt, 1984: A parameterization of the particle size spectrum of ice clouds in terms of ambient temperature and the ice water content. *J. Atmos. Sci.,* **41,** 846–855.

——, and L. J. Donner, 1990: A scheme for parameterizing ice-cloud water content in general circulation models. *J. Atmos. Sci.,* **47,** 1865–1877.

——, and G. M. McFarquhar, 1996: High albedos of cirrus in the tropical Pacific warm pool: Microphysical interpretations from CEPEX and from Kwajalein, Marshall Islands. *J. Atmos. Sci.,* **53,** 2424–2451.

——, S. Lewis, A. Bansemer, J. Iaquinta, L. M. Miloshevich, M. Kajikawa, C. Twohy, and M. R. Poellot, 2002: A general approach for deriving the properties of cirrus and stratiform ice cloud particles. *J. Atmos. Sci.,* **59,** 3–29.

Ivanova, D., D. L. Mitchell, W. P. Arnott, and M. Poellot, 2001: A GCM parameterization for bimodal size spectra and ice mass removal rates in mid-latitude cirrus clouds. *Atmos. Res.,* **59-60,** 89–113.

Jensen, E. J., and Coauthors, 2009: On the importance of small ice crystals in tropical anvil cirrus. *Atmos. Chem. Phys. Discuss.,* **9,** 5321–5370.

Khvorostyanov, V. I., and K. Sassen, 1998a: Cirrus cloud simulation using explicit microphysics and radiation. Part I: Model description. *J. Atmos. Sci.,* **55,** 1808–1821.

——, and ——, 1998b: Cirrus cloud simulation using explicit microphysics and radiation. Part II: Microphysics, vapor and ice mass budgets, and optical and radiative properties. *J. Atmos. Sci.,* **55,** 1822–1845.

——, and J. A. Curry, 2008a: Analytical solutions to the stochastic kinetic equation of liquid and ice particle size spectra. Part I: Small-size fraction. *J. Atmos. Sci.,* **65,** 2025–2043.

——, and ——, 2008b: Analytical solutions to the stochastic kinetic equation of liquid and ice particle size spectra. Part II: Large-size fraction in precipitating clouds. *J. Atmos. Sci.,* **65,** 2044–2063.

Korolev, A. V., and G. A. Isaac, 2005: Shattering during sampling by OAPs and HVPS. Part 1: Snow particles. *J. Atmos. Oceanic Technol.,* **22,** 528–542.

Lawson, R. P., B. Baker, B. Pilson, and Q. Mo, 2006: In situ observations of the microphysical properties of wave, cirrus, and anvil clouds. Part II: Cirrus clouds. *J. Atmos. Sci.,* **63,** 3186–3203.

Liu, G., 2008: A database of microwave single-scattering properties for nonspherical ice particles. *Bull. Amer. Meteor. Soc.,* **89,** 1563–1570.

Liu, H. C., P. K. Wang, and R. E. Schlesinger, 2003: A numerical study of cirrus clouds. Part I: Model description. *J. Atmos. Sci.,* **60,** 1075–1084.

Mace, G. G., A. J. Heymsfield, and M. R. Poellot, 2002: On retrieving the microphysical properties of cirrus clouds using the moments of the millimeter-wavelength Doppler spectrum. *J. Geophys. Res.,* **107,** 4815, doi:10.1029/2001JD001308.

——, Q. Zhang, M. Vaughn, R. Marchand, G. Stephens, C. Trepte, and D. Winker, 2009: A description of hydrometeor layer occurrence statistics derived from the first year of merged Cloudsat and CALIPSO data. *J. Geophys. Res.,* **114,** D00A26, doi:10.1029/2007JD009755.

Matrosov, S. Y., A. J. Heymsfield, R. A. Kropfli, B. E. Martner, R. F. Reinking, J. B. Snider, P. Piironen, and E. W. Eloranta, 1998: Comparisons of ice cloud parameters obtained by combined remote sensor retrievals and direct methods. *J. Atmos. Oceanic Technol.,* **15,** 184–196.

McFarquhar, G. M., and A. J. Heymsfield, 1998: The definition and significance of an effective radius for ice clouds. *J. Atmos. Sci.,* **55,** 2039–2052.

——, J. Um, M. Freer, D. Baumgardner, G. L. Kok, and G. Mace, 2007: Importance of small ice crystals to cirrus properties: Observations from the Tropical Warm Pool International Cloud Experiment (TWP-ICE). *Geophys. Res. Lett.,* **34,** L13803, doi:10.1029/2007GL029865.

Min, Q., and L. Harrison, 1996: Cloud properties derived from surface MFRSR measurements and comparison with GOES results at the ARM SGP site. *Geophys. Res. Lett.,* **23,** 1641–1644.

Mitchell, D. L., 1996: Use of mass- and area-dimensional power laws for determining precipitation particle terminal velocities. *J. Atmos. Sci.,* **53,** 1710–1723.

——, 2002: Effective diameter in radiation transfer: General definition, applications, and limitations. *J. Atmos. Sci.,* **59,** 2330–2346.

——, S. K. Chai, Y. Liu, A. J. Heymsfield, and Y. Dong, 1996: Modeling cirrus clouds. Part I: Treatment of bimodal size spectra and case study analysis. *J. Atmos. Sci.,* **53,** 2952–2966.

——, P. Rasch, D. Ivanova, G. McFarquhar, and T. Nousiainen, 2008: Impact of small ice crystal assumptions on ice sedimentation rates in cirrus clouds and GCM simulations. *Geophys. Res. Lett.,* **35,** L09806, doi:10.1029/2008GL033552.

——, R. P. D'Entremont, and R. P. Lawson, 2010: Inferring cirrus size distributions through satellite remote sensing and microphysical databases. *J. Atmos. Sci.,* **67,** 1106–1125.

Nelder, J. A., and R. Mead, 1965: A simplex method for function minimization. *Comput. J.,* **7,** 308–313.

Okamoto, H., S. Iwasaki, M. Yasui, H. Horie, H. Kuroiwa, and H. Kumagai, 2003: An algorithm for retrieval of cloud microphysics using 95-GHz cloud radar and lidar. *J. Geophys. Res.,* **108,** 4226, doi:10.1029/2001JD001225.

Platt, C. M. R., 1997: A parameterization of the visible extinction coefficient of ice clouds in terms of the ice/water content. *J. Atmos. Sci.,* **54,** 2083–2098.

Rodgers, C. D., 2000: *Inverse Methods for Atmospheric Sounding: Theory and Practice*. Series on Atmospheric, Oceanic, and Planetary Physics, Vol. 2, World Scientific, 238 pp.

Sassen, K., and G. C. Dodd, 1989: Haze particle nucleation simulations in cirrus clouds, and applications for numerical and lidar studies. *J. Atmos. Sci.,* **46,** 3005–3014.

Stephens, G. L., and Coauthors, 2002: The CloudSat mission and the A-Train. *Bull. Amer. Meteor. Soc.,* **83,** 1771–1790.

Varley, D. J., 1978: Cirrus particle distribution study, Part 1. United States Air Force Surveys in Geophysics, Rep. AFGL-TR-78-0192, 71 pp.

Wang, Z., and K. Sassen, 2002: Cirrus cloud microphysical property retrieval using lidar and radar measurements. Part I: Algorithm description and comparison with in situ data. *J. Appl. Meteor.,* **41,** 218–229.

Westbrook, C. D., R. J. Hogan, A. J. Illingworth, and E. J. O'Connor, 2007: Theory and observations of ice particle evolution in cirrus using Doppler radar: Evidence for aggregation. *Geophys. Res. Lett.,* **34,** L02824, doi:10.1029/2006GL027863.

Zhang, Y., and G. Mace, 2006: Retrieval of cirrus microphysical properties with a suite of algorithms for airborne and spaceborne lidar, radar, and radiometer data. *J. Appl. Meteor. Climatol.,* **45,** 1665–1689.

Zhdanov, M., 2002: *Geophysical Inverse Theory and Regularization Problems*. Elsevier, 609 pp.